Check for updates

Influences of intergrowth structure construction on the structural and electrical properties of the BBT–BiT ceramics

Yuying Wang, Deyi Zheng*, Runyu Mao and Xu Wang

College of Materials and Metallurgy, Gui Zhou University, Guiyang, China

Bismuth Layer Structured Ferroelectrics (BLSFs) have always been an important research direction of high Curie temperature piezoelectrical ceramics, and the construction of intergrowth structure has been considered as an effective method to improve the electric properties of BLSFs. There are many literatures about intergrowth structure improving electrical performance, but few reports analyze the influence of the construction of intergrowth structure on the internal defects and electrical properties in BLSFs. In this study, $(1-x)$ $BaBi_4Ti_4O_{15}$ - x $Bi_4Ti_3O_{12}$ ceramic samples with intergrowth bismuth layer structure were fabricated by a conventional solid-state reaction method, and the mechanism of the influence of intergrowth structure construction on the structure and electrical properties of BLSFs has been discussed. The crystal structure, phase composition, microstructure, dielectric and piezoelectric performance, relaxation behavior and AC conductivity of ceramic samples were systematically investigated. It has been found that the construction of intergrowth structure can significantly inhibit the generation of oxygen vacancies. The concentration of the oxygen vacancies plays an important role, and its reduction will lead to the inhibition of grain growth and the increase of the relaxation activation energy of ceramics. In addition, the intergrowth structure construction also affects the symmetry of ceramics in the c-axis direction, thus affecting the electrical properties of ceramics.

KEYWORDS

curie temperature, BBT-BiT, intergrowth structure, oxygen vacancy, electric properties

1 Introduction

The Aurivillius family of bismuth-layer structure ferroelectrics (BLSFs) as a promising candidate for high-temperature piezoelectric sensors is a development trend of piezoceramics in the future to overcome the high temperature working environment and enhance the applications in extreme environments (Wang, C. M et al., 2008; Zhang L. N et al., 2005). For example, $Bi_4Ti_3O_{12}$ (referred to as BiT) is the first choice of

piezoelectric material for high temperature piezoelectric vibration sensor (˃ 500°C) in the world at present, which is widely used in aerospace, nuclear energy and other fields to monitor the vibration of key equipment under high temperature and harsh environment (Zhang and Yu, 2011). The crystal structure of BLSFs is formed by pseudo-perovskite blocks $(A_{m-1}B_mO_{3m+1})^{2-}$ and bismuth layers $(Bi_2O_2)^{2+}$ in regular alternate arrangement (Wong et al., 2017), where A is a mono-, di-, tri-valent (Na^+, Ba^{2+}, Sr^{2+}, Ca^{2+}, Bi^{3+}, La^{3+}, etc.) cations allowing 12-coordination, B is a six- coordination transition metal (Ti^{4+}, Ta^{5+}, Nb^{5+}, Mo^{6+}, W^{6+}, Co^{3+}, etc.) and m represents the number of octahedral layers (Hou et al., 2010; Li et al., 2019).

$Bi_4Ti_3O_{12}$ (BiT, m = 3), the vital archetype of BLSFs, which has a higher Curie temperature (T_c) of 675°C and strong ferroelectric polarization (Park et al., 1999). However, the BiT ceramics has a lower piezoelectric activity, the piezoelectric constant (d_{33}) is less than 8 pC/N (Hou et al., 2010; Xie et al., 2019). The BiT ceramic has an excellent piezoelectric constant (d_{33}) of 20 pC/N and a large remnant polarization ($2P_r$) above 18 μC/cm² compared with other BLSFs ceramics after doping modification (Bokolia et al., 2015; Tang et al., 2018; Xie et al., 2019). $BaBi_4Ti_4O_{15}$ (BBT, m = 4), a class of typical bismuth layer structure piezoceramics, showing a Curie temperature T_c value of 410°C, but the piezoelectric constant at a low level, about 7 pC/N (Qi et al., 2019). The piezoelectricity and ferroelectricity of BLSFs ceramics are undesirable, because easily evaporation of bismuth element at high temperature, forming oxygen vacancies to balance the charges (Jiang et al., 2020a). Thus, the applications of BLSFs are limited by their low piezoelectric activity, and the properties of BLSFs are usually improved by ions doping, construction of intergrowth structure, and preparation process adjustment.

The intergrowth BLSFs with relatively large values of remanent polarization (P_r) are promising candidates to optimize the performance of BLSFs ceramics, which are composed of one-half the unit cell of an m member structure and one-half the unit cell of an m + 1 member structure (Noguchi et al., 2000; Yu et al., 2020). Kobayashi et al. (2004) studied that the T_c of the BBT-BiT (540°C) ceramics was between those of BiT (675°C) and BBT (410°C), and the value of spontaneous polarization (P_s = 52 μC/cm²) was larger than those of BiT and BBT ceramics. Ta^{5+} doped BBT-BiT intergrowth ceramics, the $BaBi_8(Ti_{0.995}Ta_{0.005})_7O_{27}$ showed an optimal piezoelectric performance with a d_{33} of 19 pC/N of a T_c about 475°C (Jiang et al., 2020b). And the introduction of $(Li_{0.5}Bi_{0.5})^{2+}$ ions into the BBT-BiT intergrowth ceramics increased the d_{33} from 8 to 18.5 pC/N and T_c from 480 to 633°C (Jiang et al., 2020a).

To improve the piezoelectric constant of BLSFs, the research on modification of BLSFs by synthesis techniques, ions doping and development of intergrowth structures have been highlighted by many researchers. There are many reports on the modification of BLSFs by constructing intergrowth structure, such as ions doped into intergrowth BLSFs (X. P. Jiang and Z. L.

Jiang et al., 2020a; Jiang et al., 2020b) and component regulatory of intergrowth BLSFs (Kobayashi et al., 2004; B. Wu et al., 2018). However, few reports to analyze the micro mechanism of the influence of intergrowth structure construction on the internal defects of BLSFs and the reasons why these internal defects affect the electrical properties of BLSFs. In this study, the $(1-x)$ $BaBi_4Ti_4O_{15}$—x $Bi_4Ti_3O_{12}$ (x = 0, 0.2, 0.4, 0.6, 0.8, 1) ceramics were prepared, our efforts were made to construct intergrowth structure and investigate the effect of intergrowth structure on microstructure and properties of $(1-x)$ BBT—x BiT intergrowth ceramics with different content of $Bi_4Ti_3O_{12}$. The results of XPS analysis and the calculated values of relaxation activation energy were used to analyze the effect of intergrowth structure on the oxygen vacancy concentration of ceramics. And the dielectric and piezoelectric properties study, AC impedance and conductivity analysis were used to study the micro mechanism of intergrowth structure improving electrical properties and investigated the influence rules of intergrowth structures on the microstructure and relaxation behavior of ceramics.

2 Experimental procedures

The $(1-x)$ $BaBi_4Ti_4O_{15}$ - x $Bi_4Ti_3O_{12}$ (x = 0, 0.2, 0.4, 0.6, 0.8, 1) intergrowth ceramics were synthesized by a traditional solid-state reaction, which using metal oxides of $BaCO_3$ (99%), Bi_2O_3 (99.999%) and TiO_2 (98%). Bi_2O_3 exceeds 3 wt% to compensate for its evaporation at high temperature. All raw materials were ball-milled for 16 h and calcined at 810—850°C for 3 h, then sintered at 1020°C for 2 h after pressing the pre-sintered powders into Φ 12 × 1 mm pallets. The composition and crystal lattice of the samples were analyzed by X-ray diffraction (XRD, Model XPERT-PRO) with Cu Ka radiation. The microstructures were studied by Field emission scanning electron microscope (FE-SEM, Model JSM-5900). The grain size of all ceramics was calculated via the software of nano measure, and the bulk density (ρ_b) of the ceramics was measured by the Archimedes method using a Solid Electronic Densimeter of Model MH-120C via the calculation of weight/volume. The transmission electron microscopy (TEM) was analyzed on a FEI Talos F200X system, while the X-ray photoelectron spectroscopy (XPS) was done using a Thermo ESCALAB 250XI spectrometer. Then, the piezoelectric constant (d_{33}) was measured by a ZJ quasistatic piezo-d_{33} m (Model ZJ-3A) after poling in silicone oil at 50°C under a direct current (DC) electric field of 8–10 kV/mm for 15 min, and the dielectric loss (tan δ) was tested by an LCR tester (Model TH2618B). In addition, hysteresis loops (P–E) were measured at 10 Hz with a ferroelectric tester (Aixact TF Analyzer 2000), dielectric analysis at temperature (30—700°C) and impedance analysis at frequency (20 Hz–10 MHz) were also carried out via Wayne Kerr 6500B Impedance Analyzer (WK 6500B).
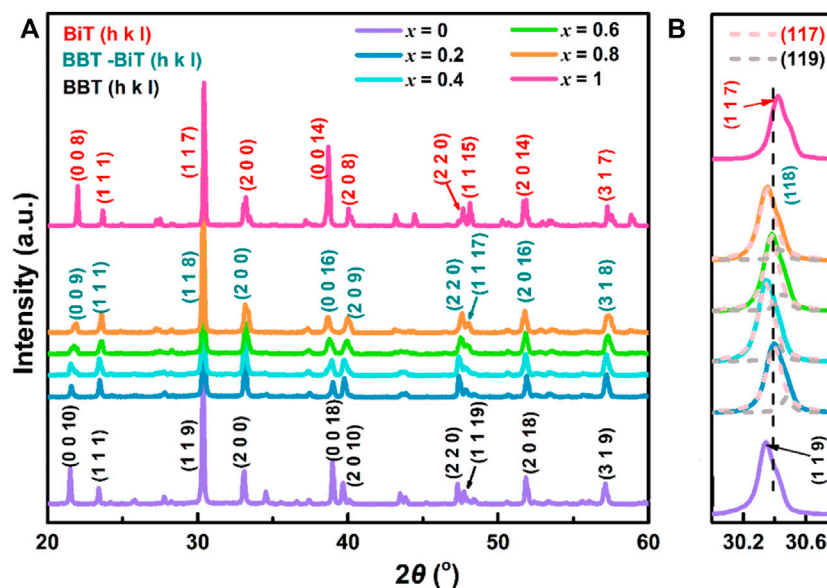
FIGURE 1
(Color online) **(A)** The room temperature XRD patterns showing the peak intensity relative to (1-*x*) BBT - *x* BiT ceramics in the 2θ range 20°−60°, **(B)** variation in the XRD peaks of BBT (119), BBT-BiT (118) and BiT (117).

3 Results and discussion

3.1 Structural and morphological characterization

The composition and crystal lattice of the (1-*x*) $BaBi_4Ti_4O_{15}$—*x* $Bi_4Ti_3O_{12}$ samples with a certain sintering temperature of 1020°C, the X-ray diffraction test are exhibited in Figure 1, *x* = 0–1. The results show that all diffraction peaks are in perfect agreement with the orthorhombic structure of BBT-BiT phase of intergrowth bismuth layered structure (BLSFs) with space group P2$_1$am and no obvious second phase (Kobayashi et al., 2004; Wang W et al., 2008). Figure 1B shows the variation in the XRD peaks of BBT (119), BBT-BiT (118) and BiT (117) at 2θ = 30.2–30.6°, the dashed lines represent the peaks of Lorentzian profile function fitting. BBT with space group A2$_1$am (*m* = 4, orthorhombic, JCPDS No. 35–0757) has the strongest peak (119), and BiT with space group B2cb (*m* = 3, monoclinic, JCPDS No. 72–1019) has the strongest peak (117). Although the position of X-ray diffraction peak shifts with the change of BiT content, the strongest peaks (118) of BBT-BiT (*m* ∼ 3.5, JCPDS No. 42–0053) are consistent with the crystal plane index (112*m* + 1) of the strongest peak in intergrowth BLSFs ceramics (Wang et al., 2010; Badapanda et al., 2019; Jiang et al., 2020a), which lie between the strongest peak (119) BBT and the strongest peak (117) of BiT. In addition, the peaks of BBT-BiT with the same Angle as that of BBT and BiT, but the peak intensity of BBT-BiT is lower than that of BBT and BiT. This

indicates that the crystallinity of BBT-BiT is lower than that of BBT and BiT ceramics, and the conductivity of BBT- BiT ceramics is lower than that of BBT and BiT ceramics, which will be proved in the subsequent analysis.

Figure 2 shows the SEM images and grain sizes distribution on fracture surfaces of (1-*x*) BBT—*x* BiT ceramics with *x* = 0 (a), 0.2 (b), 0.4 (c), 0.6 (d), 0.8 (e) and 1 (f). Due to the high grain growth rate perpendicular to the *c*-axis during grain growth of bismuth layered compounds, all samples showed the typical plate-like grains typical random lamellar grain orientation and obvious anisotropy in grain structure (Suarez et al., 2001; Diao et al., 2013). The images also exhibit that most pores on the grain boundary rather than internal grain, which indicate that ceramics sintering is relatively dense. At the same time, the grain size of BiT ceramics is extremely larger than that of BBT ceramics, while BBT-BiT samples forming intergrowth structure that the two type of perovskite layers are interlaced and symbiotic along the *c*-axis (Luo et al., 2001). In addition, the SEM images also show that the BBT-BiT intergrowth ceramics have more holes and their grains growth are not sufficiently compared with those of the single BBT and single BiT ceramics.

Figure 3A exhibits the evolutions in bulk density (ρ_b) as *x* value increase in (1-*x*) BBT—*x* BiT ceramics. The bulk density (ρ_b) of (1-*x*) BBT—*x* BiT ceramics increases with the *x* increasing, it may be caused by the differences in BBT and BiT ceramics systems. Figure 3B shows the average grain size of (1-*x*) BBT—*x* BiT ceramics. As mentioned in the XRD analysis that BBT-BiT ceramics have low crystallinity, which is usually shown as small grain size in SEM
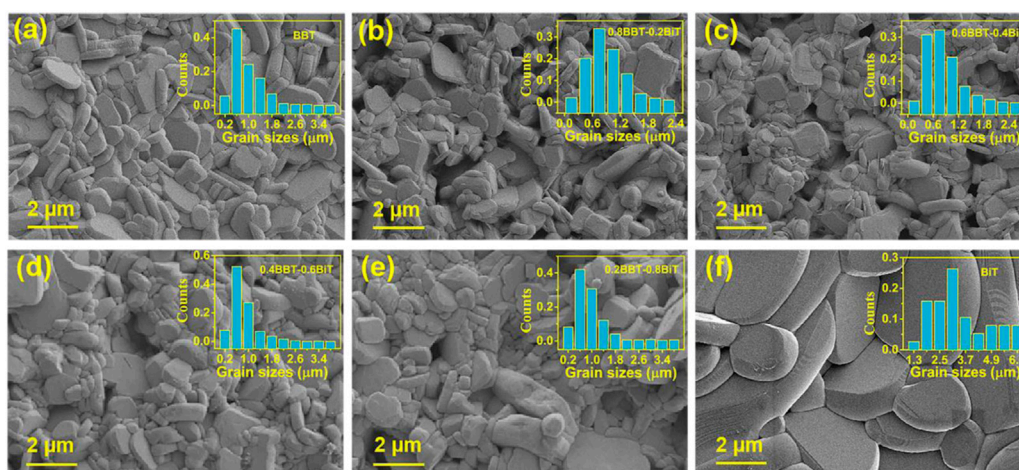
FIGURE 2
SEM images of (1-*x*) BBT—*x* BiT ceramics at a sintering temperature of 1020°C: **(A)** BBT, **(B)** 0.8BBT-0.2BiT, **(C)** 0.6BBT-0.4BiT, **(D)** 0.4BBT-0.6BiT, **(E)** 0.2BBT-0.8BiT, and **(F)** BiT.
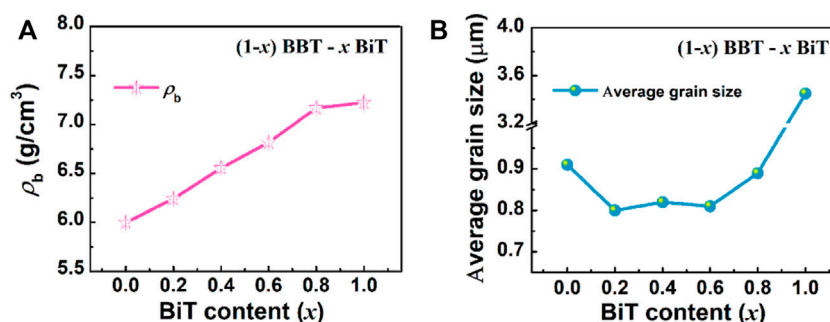

FIGURE 3
Evolutions in bulk density (ρ_b) and average grain size as *x* value increase in (1-*x*) BBT - *x* BiT ceramics: **(A)** bulk density (ρ_b), and **(B)** average grain size.

images. The average grain sizes of (1-*x*) BBT—*x* BiT (*x* = 0.2–0.8) ceramics are lower than those of BBT and BiT ceramics, combined with SEM images, these results indicate that the diffusion mechanism of BBT-BiT intergrowth ceramics play a role in the sintering process and inhibit the grain growth of the ceramic samples.

Figure 4 shows the TEM images and schematic crystal structure of the 0.8BBT-0.2BiT ceramics. Figure 4A exhibits its cross-sectional TEM image, Figures 4B, D are the high-resolution cross-sectional TEM image. Figure 4C is the FFT image of Figure 4B, which shows the that both BBT and BiT phases coexist in the sample. Figures 4E, F are partial larger version of Figures 4D, F is a figure with increased contrast after color adjustment of Figure 4E, and Figure 4G is a partial larger version of Figure 4E. Figure 4F shows an irregular layered structure with alternating layers of three and four layers, and the layer spacing values are very close to half the length of the *c*-axis of three layers (3.3 nm) or four layers (4.2 nm). BBT ceramics are composed of bismuth oxygen layer $(Bi_2O_3)^{2+}$ and four-layer pseudo-perovskite blocks $[(Ba_{1/3}Bi_{2/3})_3Ti_4O_{13}]^{2-}$ regularly alternating, while BiT ceramics are composed of bismuth oxygen layer $(Bi_2O_3)^{2+}$ and three-layer pseudo-perovskite blocks $(Bi_2Ti_3O_{10})^{2-}$ regularly alternating. Combine Figures 4F, G, the schematic crystal structure of 0.8BBT-0.2BiT ceramics are formed by irregularly alternate arrangement of bismuth oxygen layer $(Bi_2O_3)^{2+}$ and pseudo-perovskite blocks of three layers $(Bi_2Ti_3O_{10})^{2-}$ or four layers $[(Ba_{1/3}Bi_{2/3})_3Ti_4O_{13}]^{2-}$.

3.2 Dielectric and piezoelectric performance analysis

Figure 5 shows the temperature dependence of the dielectric constant ε_r for all samples from 30°C to 700°C at five frequencies
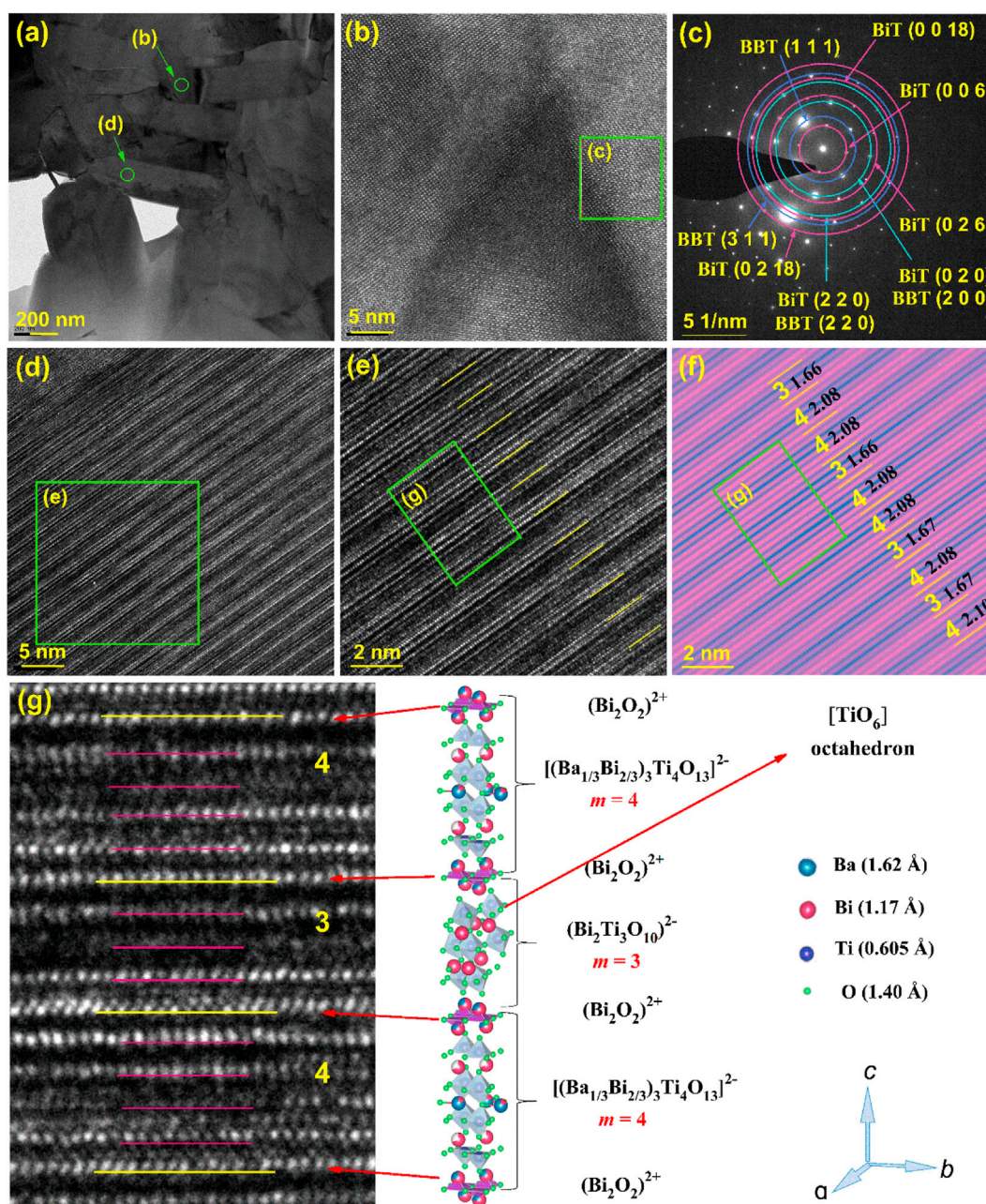
FIGURE 4
TEM images and schematic crystal structure of the 0.8BBT-0.2BiT ceramics: **(A)** Cross-sectional TEM image, **(B)** high-resolution Cross-sectional TEM image, **(C)** FFT image of Figure 4 **(B,D)** high-resolution Cross-sectional TEM image, **(E)** a partial larger version of Figure 4 **(D,F)** high contrast view with layer spacing of Figure 4 **(E,G)** a partial larger version of Figure 4 **(E)** with its schematic crystal structure.

as color online. It can be seen from ε_r—T curves of all samples at these frequencies, the dielectric constants decrease with increasing frequency (that is phenomenon of frequency dispersion) and the peak of dielectric constants occur near Curie temperature T_c. The T_1 temperature of BiT ceramics in Figure 5F indicates that the sample has undergone phase transformation in the vicinity of this temperature. The flat dielectric constant in relation to temperature of relaxation ferroelectrics is due to the presence of polar nanoregions on the structure, which makes them in ergodic relaxor state (Ni et al., 2013). Meanwhile, the values of Curie temperature change at different frequencies and T_c increase with increasing
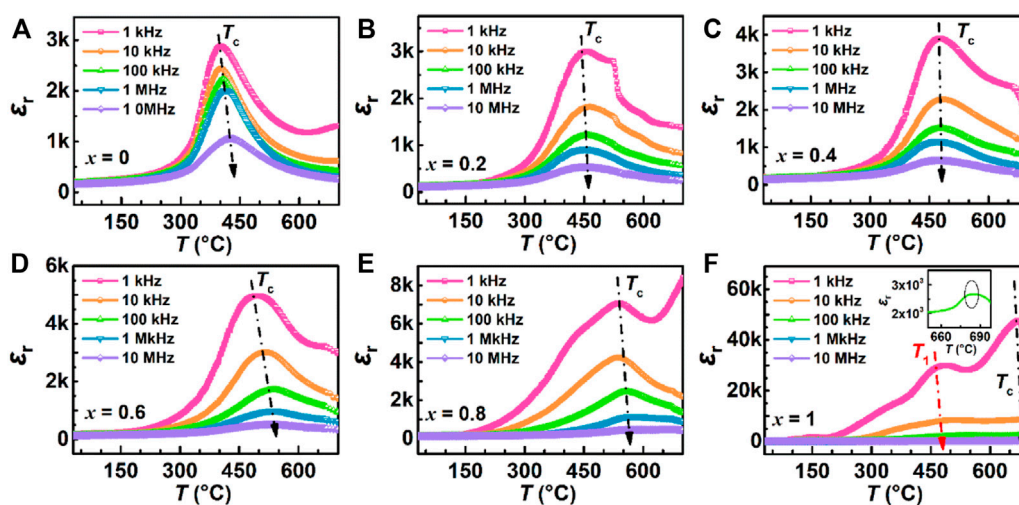
FIGURE 5
(Color online) Temperature dependence of dielectric constant for (1-*x*) BBT - *x* BiT ceramics at different frequencies (1 kHz−10 MHz): **(A)** BBT, **(B)** 0.8BBT-0.2BiT, **(C)** 0.6BBT-0.4BiT, **(D)** 0.4BBT-0.6BiT, **(E)** 0.2BBT-0.8BiT, and **(F)** BiT.
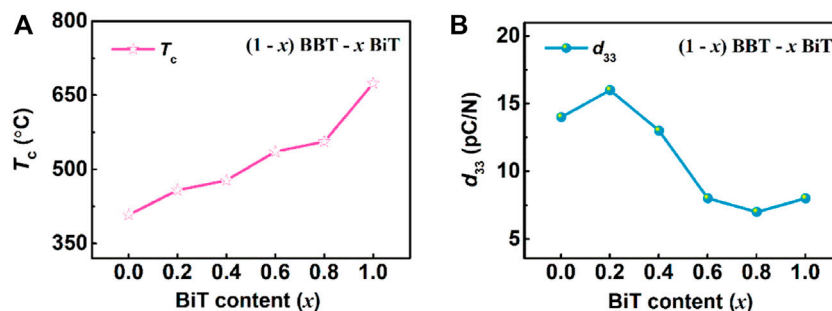

FIGURE 6
(Color online) The variation of Curie temperature T_c, piezoelectric constant d_{33}, coercive field E_c and remnant polarization P_r for (1-*x*) BBT—*x* BiT ceramics with different BiT content (*x*): **(A)** T_c, **(B)** d_{33}.

frequency generally, except in Figures 5B, C. Due to the influence of space charge and conductivity, the dielectric constant tends to increase at low frequency and high temperature (Wang et al., 2022), so 100 kHz is selected as a frequency for subsequent experimental analysis.

Figure 6 exhibits the curves of Curie temperature T_c and piezoelectric constant d_{33} of (1-*x*) BBT—*x* BiT ceramics with different BiT content (*x*), respectively. As the T_c—*x* curve at 100 kHz shown in Figure 6A, the Curie temperatures T_c (458–556°C) of BBT-BiT intergrowth ceramics are between BBT (408°C) and BiT (674°C), which increase with the increase of BiT content *x*. Lattice distortion is the main influencing factor of Curie temperature (T_c) of bismuth layered ceramics, which can be expressed by tolerance factor (*t*), as shown in law (Eq. 1) (Suarez et al., 2001).

$$t = \frac{(R_A + R_O)}{\sqrt{2}(R_A + R_O)} \tag{1}$$

where, R_A, R_A and R_O are the ionic radii of A-site, B-site and O^{2-} respectively. The smaller the tolerance factor *t*, the higher the Curie temperature T_c of the ceramics. At this work, the general formula is $(Bi_2O_2)^{2+}(A_{m-1}B_mO_{3m+1})^{2-}$ for bismuth-layered structure ferroelectrics (BLSFs), the B-site is occupied by Ti^{4+} with an ionic radius of 0.605 Å, while the A-site is Bi^{3+} with an ionic radius of 1.17Å for $Bi_4Ti_3O_{12}$ (BiT) ceramics and A-site is $(Ba_{1/3}^{2+} Bi_{2/3}^{3+})$ for $BaBi_4Ti_4O_{15}$ (BBT) ceramics with an ionic radius of 1.32 Å. Thus, the radius of A site ion for (1-*x*) $BaBi_4Ti_4O_{15}$ - *x* $Bi_4Ti_3O_{12}$ intergrowth ceramics decreases with the increase of BiT content (*x*). With the increase of *x*, the increase of radius of A-site leads to decrease *t*, so T_c gradually
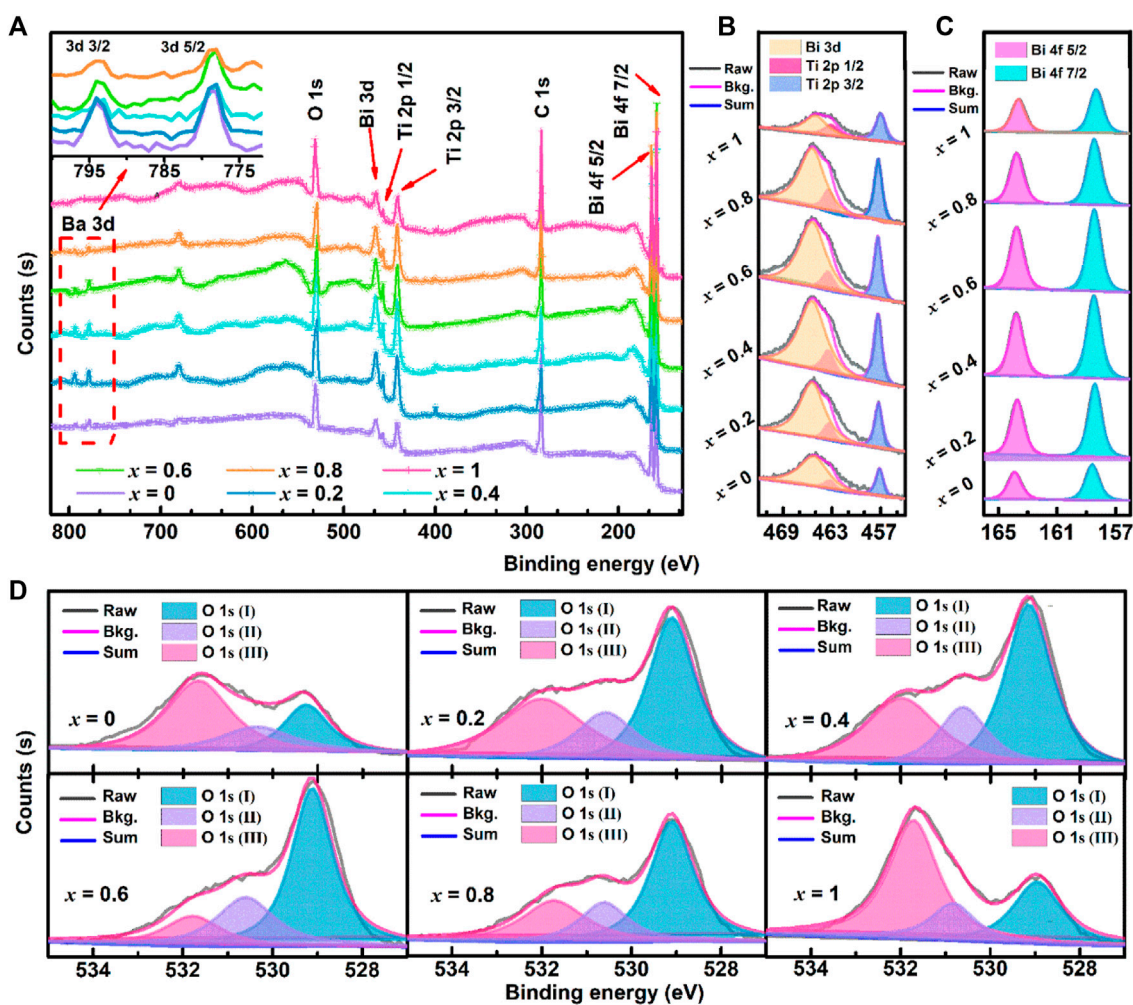
FIGURE 7
(Color online, Bkg. is short for Background) XPS spectra for (1–x) BBT—x BiT ceramics with different BiT content (x): **(A)**, XPS Survey, **(B)** O 1s scan, **(C)** Bi 4f scan, and **(D)** Bi 3 days and Ti 2p scan.

increases, indicating that the BBT-BiT intergrowth structure of BLSFs increase Curie temperature compared with single BBT ceramics.

As shown in Figure 6B, the piezoelectric constants d_{33} increase first and then decrease with the increase of x of BBT-BiT intergrowth ceramics, show an opposite trend in changes, compared with that of T_c. The intergrowth structure of BLSFs with $m/m+1$ layers are composed of m layers and $m+1$ layers, two-phase lattice distortion occurs due to the mismatch of lattice parameters, resulting in the formation of new intergrowth structural phases to match the lattice (Yang et al., 2018). The intergrowth structure, which affects the symmetry of ceramic c-axis direction and the properties of material. And the intergrowth structure construction also effects oxygen vacancy concentration, which will affect the deflection of ferroelectric domains, thus affecting the piezoelectric properties of BBT-BiT

ceramics. At the same time, the maximum value of d_{33} for BBT-BiT ceramics is obtained at x = 0.2, the piezoelectric constant d_{33} is 16 pC/N and its corresponding Curie temperature T_c is 458°C. Combined with the SEM results, it can be found that the BBT-BiT intergrowth ceramic (especially 0.8BBT-0.2BiT sample) are with smaller grain size and more pores than the BBT and BiT samples. Therefore, the oxygen vacancy concentration can be controlled through many methods, such as ions doping and vacuum sintering, to further improve the grain growth and electrical properties.

3.3 XPS spectra study

Figure 7 shows the XPS survey spectra and O 1s scan of (1-x) BBT—x BiT ceramics. As shown in Figure 7A, the resolution

TABLE 1 Bind Energy, Peak Area and its Area percentage content of oxygen peaks, and ratio of $O_{Non-lattice}/O_{Lattice}$ for all samples.

BBT-*x*BiT		*x* = 0	*x* = 0.2	*x* = 0.4	*x* = 0.6	*x* = 0.8	*x* = 1
O^{2-}	B. E. (eV)	529.29	529.08	529.15	529.12	529.10	528.95
	Area	23598.27	69507.45	80410.92	77039.91	61366.95	35073.94
	Area %	26.66	46.78	50.46	58.89	53.23	28.68
O^2/O^-	B. E. (eV)	530.38	530.49	530.56	530.60	530.61	530.83
	Area	17173.21	29346.75	29817.38	33770.72	22651.98	19011.79
	Area %	19.40	19.75	18.71	25.82	19.65	15.54
O1s	B. E. (eV)	531.68	531.98	531.95	531.78	531.73	531.71
	Area	47730.11	49721.93	49113.4	20003.07	31261.56	68223.16
	Area %	53.93	33.47	30.82	15.29	27.12	55.78
$O_{Non-lattice}/O_{Lattice}$		2.75	1.14	0.98	0.70	0.88	2.49

spectrum of Bi 3 days has 3 days 3/2 and 3 days 5/2 doublets in the binding energy range of 800–770 eV, and the change of peak area reflects the decrease of Ba 3 days content with the increase of BiT content (*x*). Bi 4f, Bi3d and Ti 2p spectra increase first and then decrease in the peak areas as shown in Figures 7B, C. For (1-*x*) BBT - *x* BiT intergrowth ceramics (*x* = 0.2–0.8), the binding energy of Bi 4f, Bi3d and Ti 2p shift not significantly with the *x* increasing, compared with those of BBT and BiT ceramics, which also shows that the intergrowth bismuth layered ceramics did not generate other impurity phases.

To further confirm the sources of oxygen vacancy in the samples, the peaks of O 1s scan are fitted into three peaks as shown in Figure 7D. Take BBT ceramics for example, the Lattice oxygen ions ($O_{Lattice}$) are represented as O 1s (I) peak (529.29 eV), the None-lattice oxygen ions ($O_{Non-lattice}$) are represented as O 1s (II) peak (530.38 eV) induced by oxygen deficiency from deviation of $BaBi_4Ti_4O_{15}$ stoichiometric ratio in oxygen defect region and the O 1s (III) peak (531.68 eV) generated by the organic oxygen from the circumstance of the samples' surface (Yoo et al., 2012; Jaim et al., 2017; Reddy et al., 2019). Table 1 shows the values of the integral Area and Area percentage content of oxygen peaks from the above different sources, and the ratio of $O_{Non-lattice}/O_{Lattice}$.

Bismuth volatilizes easily at a high sintering temperature of 1000–1100°C for BLSFs, resulting in forming Bi vacancies (V_{Bi}''') and oxygen vacancies ($V_O^{\bullet\bullet}$) that can be expressed by Kröger–Vink formula (2) (Qiao et al., 2016):

$$2Bi_{Bi}^{\times} + 3O_O^{\times} \Leftrightarrow Bi_2O_3 \, (gas) + 2V_{Bi}''' + 3V_O^{\bullet\bullet} \qquad (2)$$
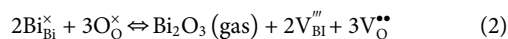
where $Bi_{Bi}^{\times}$ and $O_O^{\times}$ present electrically neutral vacancy of Bi and O, respectively. According to the $O_{Non-lattice}/O_{Lattice}$ values of the (1 − *x*) BBT − *x* BiT ceramics in Table 1, there are more oxygen vacancy defects in single BBT (2.75) and BiT (2.49) BLSFs, indicating that the intergrowth structure of BLSFs can inhibit the generation of oxygen vacancies. Oxygen vacancies promote ions to diffusion and

transfer during sintering, improving the sintering speed of ceramics to promote the growth of grains (Tewari et al., 2014; Tang et al., 2020), which are also consistent with the SEM images (Figure 2) and average grain size (Figure 3B) results.

3.4 Impedance analysis

Figure 8 shows Z′-Z″ complex impedance spectra collected under various temperatures with the frequency of 100 Hz–10 MHz, the impedance spectra selected the temperature range of the impedance circle that can be obtained by the sample. These Z′-Z″ spectra are fitted with the equivalent circuit as shown in Figure 8A, which can be composed of approximately two superimposed semicircles, reflecting the impedance contribution of the grain (high-frequencies arc) and grain boundary (low-frequencies arc) to the materials (Dhak et al., 2008). Figures 8A–E show that the Z′-Z″ spectra of ceramics are approximately single semicircles, which mainly represent the dominant role of grain boundary characteristics, and the interaction between grain, grain boundary and ceramic electrode interface (Lin and Chen, 2009). Moreover, the BiT ceramic exhibits grain and grain boundary characteristics as shown in Figure 8F.

For all samples, the radius of curvature decreases with increasing temperature for the Z′-Z″ complex impedance spectra, indicating that the resistivity of the sample has a negative temperature coefficient (Fujii et al., 2002). Meanwhile, Z′ decreases gradually with the increase of BiT content at the same temperature. Asymmetric in all characteristic wide peaks at measured temperatures for all samples indicates non-Debye type relaxation processes (Pradhani et al., 2018), and the values of resistance, capacitance and relaxation time for the bulk and grain boundary was listed in Table 2.
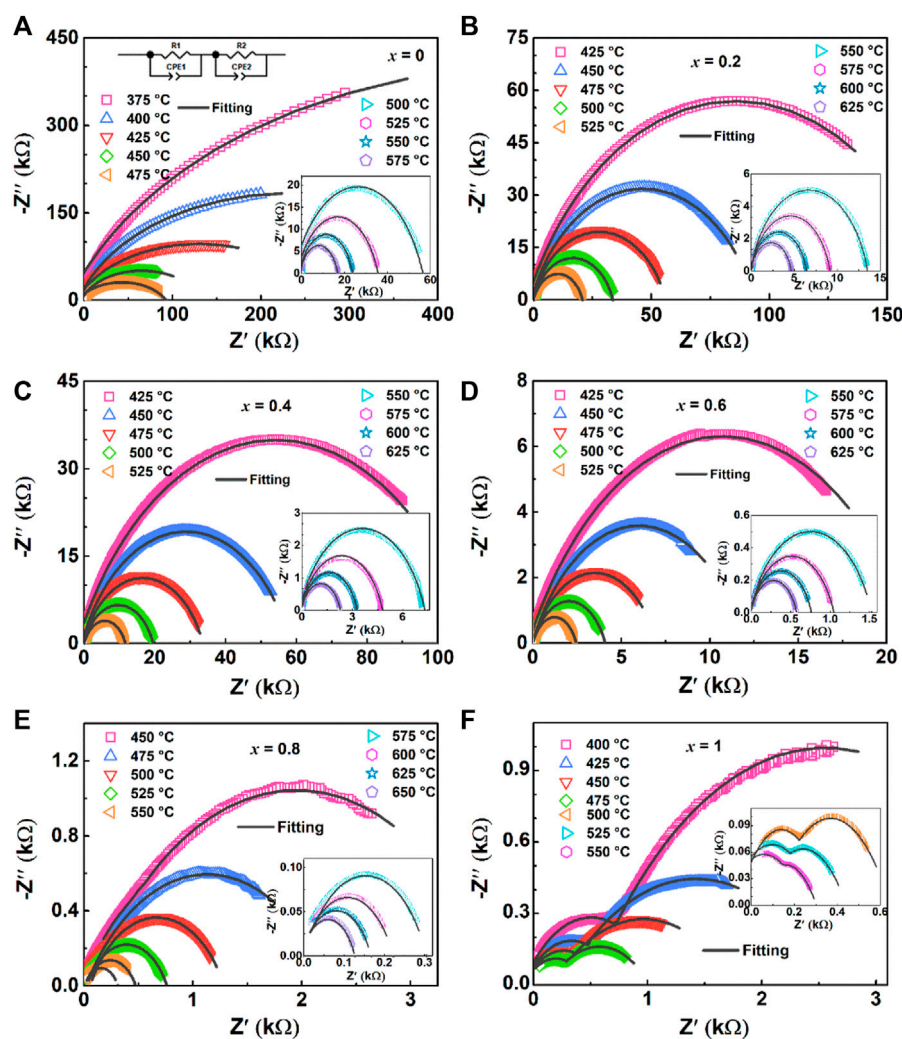
FIGURE 8
(Color online) Complex impedance spectra for (1-x) BBT—x BiT ceramics at various temperatures: **(A)** BBT, **(B)** 0.8BBT-0.2BiT, **(C)** 0.6BBT-0.4BiT, **(D)** 0.4BBT-0.6BiT, **(E)** 0.2BBT-0.8BiT, and **(F)** BiT.

To confirm the relaxation mechanisms of the ceramics, relaxation frequencies (ω_{max} (T)) in relation to temperature ln ω - $1/T$ are plotted in Figure 9. The relaxation activation energy (E_{relax}) is calculated by Arrhenius equation according to the slopes obtained from the linear fitting of the plots, this law (Eq. 3) as follow (Qiao et al., 2016):

$$\omega_{max}(T) = \omega_0 \exp\left(-\frac{E_{relax}}{k_B T}\right) \quad (3)$$

where T is the temperature in Kelvin scale, ω_0 is the pre-exponential factor, and k_B is the Boltzmann constant.

Figure 9 shows ln ω - $1/T$ relaxation frequency Arrhenius diagram of all ceramics at different temperatures, and the values of activation energy E_{relax} (E_g and E_{gb} are relaxation activation energy

of grain and grain boundary, respectively) of the relaxation process are summarized in this figure and Table 2. The relaxation activation energy values of grains of (1-x) BBT - x BiT (x = 0–0.8) ceramics are no longer given here, because of the conduction mechanisms of these samples are mainly from the grain boundary contribution. In the thermal excited state, the oxygen vacancy will undergo single and double ionization and generate free electrons, as shown in Eq. 4 and Eq. 5 (Wu and Wang, 2010):

$$V_O \Leftrightarrow V_O^\bullet + e' \quad (4)$$

$$V_O^\bullet \Leftrightarrow V_O^{\bullet\bullet} + e' \quad (5)$$

Where V_O is unionized oxygen vacancies, e' is free electron, and $V_O^\bullet$ and $V_O^{\bullet\bullet}$ present singly and doubly ionization oxygen vacancy, respectively. In addition, the activation energy of the

TABLE 2 Fitting results of all ceramics at the temperatures of 450°C, 500°C and 550°C: Resistance (R_g), capacitance (C_g), relaxation time determined (τ_g) and relaxation activation energy (E_g) for bulk (grain); resistance (R_{gb}), capacitance (C_{gb}), relaxation time determined (τ_{gb}) and relaxation activation energy (E_{gb}) for grain boundary.

| (1-x) BBT——x BiT		R_g (kΩ)	C_g (nF)	τ_g (10^{-5} s)	E_g	R_{gb} (kΩ)	C_{gb} (nF)	τ_{gb} (10^{-5} s)	E_{gb}
x = 0	450°C	73.37	1.37	10.0420	—	130.08	1.94	25.2244	1.50
	500°C	21.75	0.70	1.5199	—	54.38	1.19	6.4837	1.50
	550°C	14.20	0.47	0.6635	—	22.89	0.66	1.5199	1.50
x = 0.2	450°C	60.20	1.83	11.0108	—	91.01	2.59	23.5407	1.32
	500°C	19.06	1.26	2.4089	—	35.18	1.89	6.6347	1.46
	550°C	0.93	0.90	0.8746	—	12.94	1.12	1.4515	1.46
x = 0.4	450°C	22.62	1.53	3.46	—	55.80	2.85	15.9155	1.30
	500°C	9.55	1.29	1.24	—	19.81	21.16	4.2837	1.59
	550°C	4.09	0.87	0.36	—	7.41	1.36	1.0042	1.59
x = 0.6	450°C	6.67	1.31	0.8746	—	12.38	2.51	3.1033	1.21
	500°C	2.80	1.46	0.4091	—	4.09	2.14	0.8746	1.21
	550°C	1.43	1.34	0.1913	—	1.57	1.50	0.2354	1.45
x = 0.8	450°C	2.69	1.63	0.4383	—	4.03	2.49	1.0042	1.32
	500°C	1.37	2.31	0.3176	—	1.27	1.99	0.2522	1.32
	550°C	0.56	2.28	0.1264	—	0.47	1.69	0.0798	1.32
x = 1	450°C	0.54	0.36	0.0196	0.43	1.92	20.79	3.9978	0.89
	500°C	0.30	0.31	0.0094	1.69	0.74	61.99	0.4590	0.89
	550°C	0.11	0.18	0.0020	1.69	0.34	16.34	0.0552	2.36
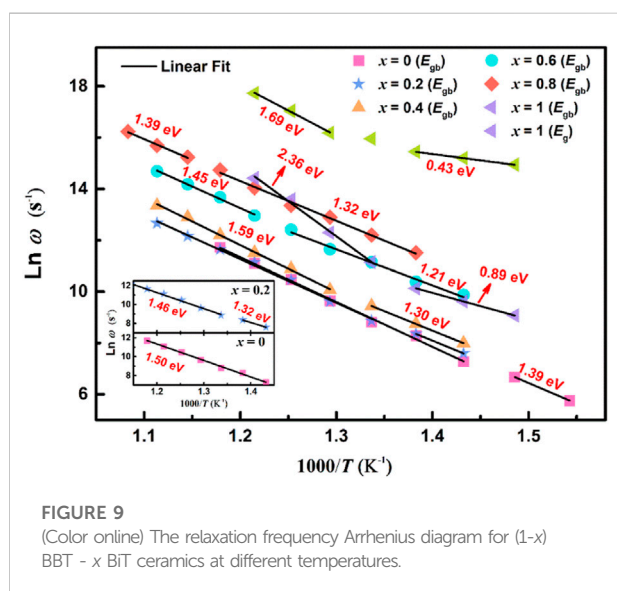
FIGURE 9
(Color online) The relaxation frequency Arrhenius diagram for (1-x) BBT - x BiT ceramics at different temperatures.

double ionized oxygen vacancy is approximately 0.6–1.2 eV, while that of the single ionized oxygen vacancy is less than 0.3–0.5 eV (Ma et al., 2021).

The BBT sample above the Curie temperature T_c (408°C) with an activation energy E_{gb} of 1.50 eV between 425 and 575°C, and the BBT sample below T_c with an activation energy E_{gb} of 1.39 eV between 375 and 400°C. This figure exhibits different conduction modes before and after ferroelectric phase transition for the (1-x) BBT - x BiT (x = 0.2–0.8) intergrowth ceramics. The activation energy values of these ceramics are lower at low temperatures and low frequencies before the ferroelectric phase transition, while the values are higher of these ceramics at high temperatures and high frequencies after the ferroelectric phase transition. These values of E_{relax} are much larger than that of oxygen vacancy activation energy (more than 1.0 eV), indicating that the movement of oxygen vacancy is no longer the main conduction mode at high temperature and the reduction of oxygen vacancy content (Steinsvik et al., 1997).

The BiT ceramics undergo phase transformation near temperature T_1 (Figure 5F) to exhibit various values of E_{relax}. At the temperature of 400–450°C, it amounts to 0.43 eV at lower frequency and 0.89 eV at higher frequency, illustrating that the conductivity mainly comes from the conductivity of single ionized oxygen vacancy at lower frequency, and the carrier migration at higher frequency is mainly manifested by oxygen vacancy overcoming potential barrier transition from high
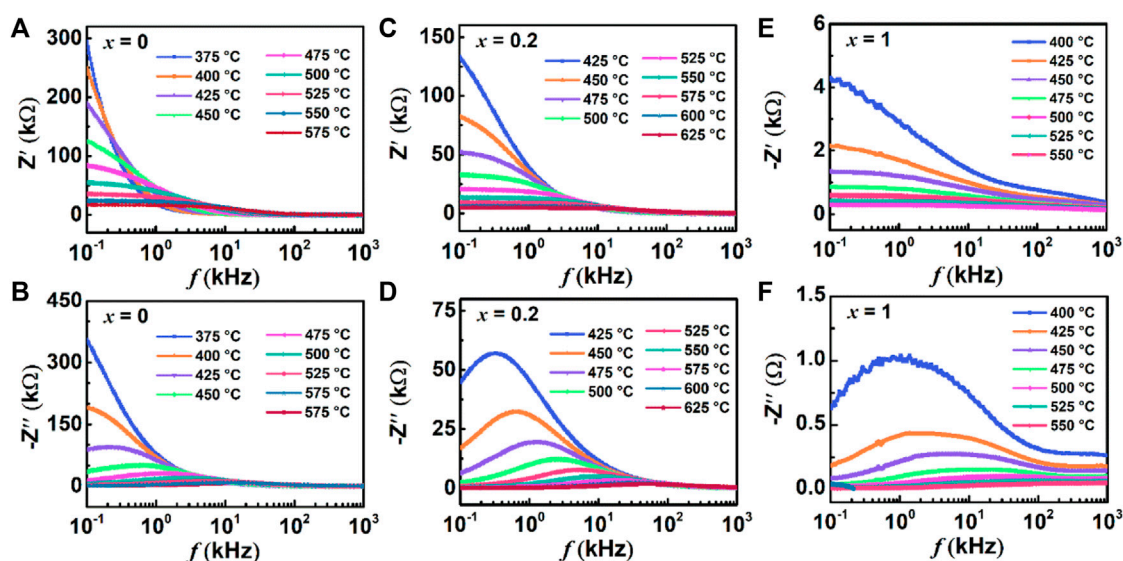
FIGURE 10
(Color online) Frequency variation of Z' and Z" from 100 Hz~1 MHz at various temperatures for(1-x) BBT - x BiT ceramics: **(A,B)** BBT **(C,D)** 0.8BBT-0.2BiT, and **(E,F)** BiT.

energy level to low energy level (Chan et al., 1982; Raymond et al., 2005). At higher temperature of 475–550°C, BiT ceramics show great values of relaxation activation energy, and the dominant modes of conduction are cationic vacancies rather than oxygen vacancy at higher temperature (Guiffard et al., 2005).

Compared with BiT ceramics, the intergrowth structure of BBT-BiT ceramics improves the activation energy of BLSFs and reduces the oxygen vacancy concentration of BLSFs. The more oxygen vacancies can increase the leakage current of the ceramics, resulting in the incomplete polarization of the ceramic and the decrease of the piezoelectric constant, which in keeping with the electric properties results (Figure 6).

Table 2 exhibits the fitting values of resistance (R_g and R_{gb}), capacitance (C_g and C_{gb}), relaxation time determined (τ_g and τ_{gb}) and relaxation activation energy (E_g and E_{gb}) for bulk and grain boundary at various temperatures of 450°C, 500°C and 550°C, respectively. The resistance and relaxation activation energy values of the grain boundary are greater than those of the grain ($R_g > R_{gb}$, $E_g > E_{gb}$), and the resistance and relaxation time of ceramics gradually decrease with the increasing of BiT content x and test temperature.

The real part of impedance responses for BBT (a), 0.8BBT-0.2BiT (c), and BiT (e) BiT, as well as imaginary part of impedance responses for BBT (b), 0.8BBT-0.2BiT (d), and BiT (f) BiT are presented in Figure 10. The amplitude of Z' decreases with increasing temperature, indicating an increase of the AC conductivity of ceramics with increasing temperature, as shown in Figures 10A, C, E (Rafiq et al., 2015). With the temperature increasing, the maximum values of Z" are shifted and broadened

at a higher frequency, which indicates the presence of relaxation processes with temperature-dependent, as shown in Figures 10B, D, F (Macdonald and Jhonson, 2005). There are two relaxation peaks at the frequency range of BiT ceramics as shown in Figure 10F, the lower and higher frequencies regions correspond to the impedance response of the grain-boundary and grain respectively.

3.5 AC conductivity analysis

To study further on the conduction mechanism of ceramics, the AC conductivity (σ_{ac}) (Majhi et al., 2009) and conductance activation energy (E_{con}) (Gupta et al., 2018) of samples conform to the following Eq. 6 and Eq. 7, respectively.

$$\sigma_{ac} = \left(\frac{Z'}{Z'^2 + Z''^2}\right)\left(\frac{d}{A}\right) \qquad (6)$$

Where d and A are the diameter and area of the sample, respectively. And the AC conductivity σ_{ac} diagrams of all samples are shown in Figure 11.

$$\sigma_{ac} = \sigma_0 \exp\left(-\frac{E_{con}}{k_B T}\right) \qquad (7)$$

Where σ_0 is the pre-exponential term. The values of conductance activation E_{con} for all samples are summarized in Figure 12.

Figure 11 shows the variation of AC conductivity and frequency of all ceramics at different temperatures. The AC
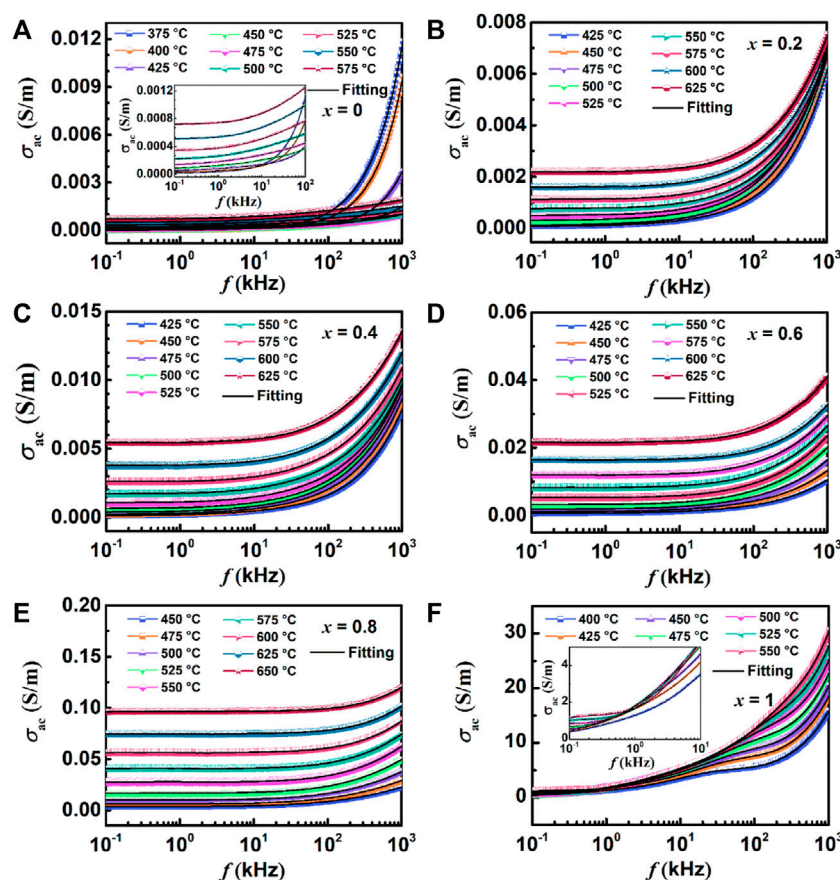
FIGURE 11
Variation of AC conductivity and frequency at different temperatures: **(A)** BBT, **(B)** 0.8BBT-0.2BiT, **(C)** 0.6BBT-0.4BiT, **(D)** 0.4BBT-0.6BiT, **(E)** 0.2BBT-0.8BiT, and **(F)** BiT.

conductivity of the (1-x) BBT - x BiT ceramics increases with x increasing, because the conductivity of BiT ceramics itself is higher than that of BBT ceramics. The values of conductivity for 0.2BBT-0.8BiT ceramics with the optimal performance are in the range of 5.6×10^{-5}–6.8×10^{-3} S/m below the curie temperature of 475°C (at frequencies of 10^2–10^6 Hz), which is lower than that of single BiT ceramics (0.85–22.74 S/m). Combined with the above analysis results, it can be concluded that the decrease of oxygen vacancy concentration has the main contribution to the decrease of ceramic conductivity. Meanwhile, the AC conductivity increases with the increase of temperature, indicating that conductance is related to thermally activated carriers (mainly oxygen vacancies and local carriers). Moreover, the conductivity of the ceramic is basically unchanged at low frequency, and the conductivity increases with increasing temperature and frequency at higher frequencies by the formation of AC conductance by the charge hopping process (Raymond et al., 2005).

Figure 12 shows the Arrhenius plots of AC conductivity of (1-x) BBT—x BiT ceramics ($x = 0$–1) at different frequencies, and the activation energy values of ceramics were calculated from the Ln σ—T linear fitting data. As for the (1-x) BBT—x BiT ceramics ($x = 0$–0.8), the values of activation energy are close to the double ionization activation energy of the oxygen vacancy at the lower frequencies of 1 kHz and 10 kHz, while the values of activation energy are close to the single ionization activation energy of the oxygen vacancy at the higher frequencies of 100 kHz and 1000 kHz. These results indicate that the conductivity mechanism is mainly related to the secondary ionization and single ionization of the oxygen vacancy at lower and higher frequencies, respectively. It also can be seen that the activation energy of BiT ceramics is very low, between 0.05 and 0.38 eV, indicating that its conductive mechanism is no longer oxygen vacancies, the conductive mechanism is probably impurity conductance (Zhang, S. J et al., 2005). Thus, the oxygen vacancies are the main carriers and the main cause of the
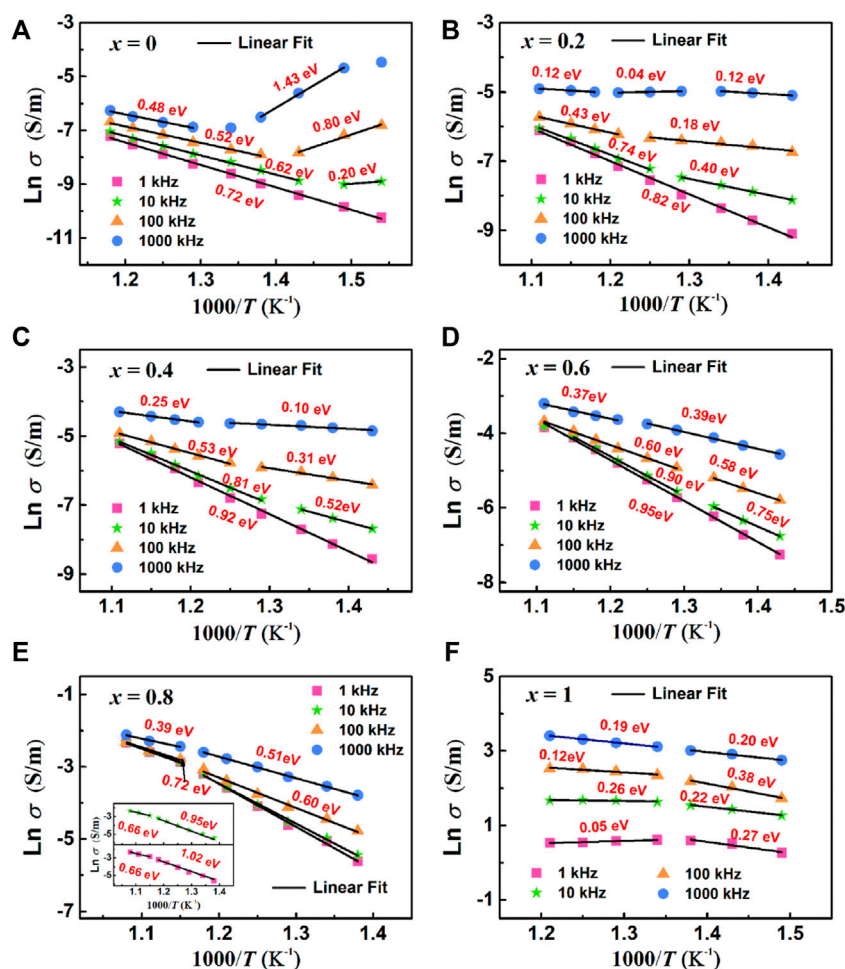
FIGURE 12
Arrhenius plots of AC conductivity at different frequency: **(A)** BBT, **(B)** 0.8BBT-0.2BiT, **(C)** 0.6BBT-0.4BiT, **(D)** 0.4BBT-0.6BiT, **(E)** 0.2BBT-0.8BiT, and **(F)** BiT.

conductivity behavior for $(1-x)$ BBT—x BiT ceramics ($x = 0$–0.8), and the conductive mechanism of BiT ceramics is probably impurity conductance.

4 Conclusion

In this study, $(1-x)$ BaBi$_4$Ti$_4$O$_{15}$—x Bi$_4$Ti$_3$O$_{12}$ ceramic samples with intergrowth bismuth layer structure were fabricated by a conventional solid-state reaction method. The results of XRD and TEM show that the BBT-BiT intergrowth ceramics formed the intergrowth structure of two kinds of perovskite layers along the c-axis, and there is no obvious second phase. The construction of this intergrowth structure leaded to a large reduction in the oxygen vacancy concentration in this samples through the XPS results, and the reduction in the oxygen vacancy concentration will inhibit grain growth as shown

in SEM results. It is also proposed that the change of oxygen vacancy concentration may affect the relaxation activation energy, the deflection of ferroelectric domains and the piezoelectrical properties. Furthermore, the intergrowth structure of BLSFs affects the symmetry of ceramic c-axis direction, which has an impact on the electrical properties of the ceramics. Based on the above influence, the 0.8BBT-0.2BiT intergrowth ceramics show the best performance: $d_{33} = 16$ pC/N, $T_c = 458°C$, $\sigma_{ac} = 5.6 \times 10^{-5}$–$6.8 \times 10^{-3}$ S/m ($T < 475°C$, $f = 10^2$–10^6 Hz).

Data availability statement

The original contributions presented in the study are included in the article/supplementary material, further inquiries can be directed to the corresponding author.

Author contributions

YW prepared the BiT-BBT intergrowth ceramics by traditional solid-phase sintering method, and performed all characterization analysis and tests for these samples. DZ contributed to the conception of the study and helped to discuss and analyze part of characterization results. RM and XW helped to prepare samples and perform a partial electrical performance test. All authors participated in the discussion of the results of this manuscript.

Funding

This project is supported by the National Natural Science Foundation of China (grant number 51762009), the Guizhou Provincial Education Department (grant number Z174043), the Guizhou Provincial Science and Technology Department [grant number QKHZC (2020) YB 080], and the Guizhou Provincial Science and Technology Department [grant number QKHJC-ZK (2021) ZD 049].

Conflict of interest

The authors declare that the research was conducted in the absence of any commercial or financial relationships that could be construed as a potential conflict of interest.

Publisher's note

All claims expressed in this article are solely those of the authors and do not necessarily represent those of their affiliated organizations, or those of the publisher, the editors and the reviewers. Any product that may be evaluated in this article, or claim that may be made by its manufacturer, is not guaranteed or endorsed by the publisher.

References

Badapanda, T., Nayak, P., Mishra, S. R., Harichandan, R., and Ray, P. K. (2019). Investigation of temperature variant dielectric and conduction behavior of strontium modified $BaBi_4Ti_4O_{15}$ ceramic. *J. Mat. Sci. Mat. Electron.* 30 (3), 3933–3941. doi:10.1007/s10854-019-00678-6

Bokolia, R., Thakur, O. P., Rai, V. K., Sharma, S. K., and Sreenivas, K. (2015). Dielectric, ferroelectric and photoluminescence properties of Er^{3+} doped $Bi_4Ti_3O_{12}$ ferroelectric ceramics. *Ceram. Int.* 41 (4), 6055–6066. doi:10.1016/j.ceramint.2015.01.062

Chan, N. H., Sharma, R. K., and Smyth, D. M. (1982). Nonstoichiometry in acceptor-doped $BaTiO_3$. *J. Am. Ceram. Soc.* 65, 167–170. doi:10.1111/j.1151-2916.1982.tb10388.x

Dhak, D., Dhak, P., and Pramanik, P. (2008). Influence of substitution on dielectric and impedance spectroscopy of $Sr_{1-x}Bi_{2+y}Nb_2O_9$ ferroelectric ceramics synthesized by chemical route. *Appl. Surf. Sci.* 254, 3078–3092. doi:10.1016/j.apsusc.2007.10.097

Diao, C. L., Xu, J. B., Zheng, H. W., Fang, L., Gu, Y. Z., and Zhang, W. F. (2013). Dielectric and piezoelectric properties of cerium modified $BaBi_4Ti_4O_{15}$ ceramics. *Ceram. Int.* 39 (6), 6991–6995. doi:10.1016/j.ceramint.2013.02.036

Fujii, Y., Soejima, Y., Okazaki, A., Bdikin, I. K., Emel'chenko, G. A., and Zhokhov, A. A. (2002). The characteristics of orthorhombicity of $YBa_2Cu_3O_{7-\delta}$ in superconducting state. *Phys. C. Supercond.* 377, 49–55. doi:10.1016/s0921-4534(01)01109-1

Guiffard, B., Boucher, E., Eyraud, L., Lebrun, L., and Guyomar, D. (2005). Influence of donor co-doping by niobium or fluorine on the conductivity of Mn doped and Mg doped PZT ceramics. *J. Eur. Ceram. Soc.* 25 (12), 2487–2490. doi:10.1016/j.jeurceramsoc.2005.03.087

Gupta, P., Padhee, R., Mahapatra, P. K., Choudhary, R. N. P., and Das, S. (2018). Structural and electrical properties of Bi_3TiVO_9 ferroelectric ceramics. *J. Alloys Compd.* 731, 1171–1180. doi:10.1016/j.jallcom.2017.10.123

Hou, J. G., Qu, Y. f., Vaish, R., Varma, K. B. R., Krsmanovic, D., and Kumar, R. V. (2010). Crystallographic evolution, dielectric, and piezoelectric properties of $Bi_4Ti_3O_{12}$: W/Cr ceramics. *J. Am. Ceram. Soc.* 93 (5), 1414–1421. doi:10.1111/j.1551-2916.2009.03582.x

Jaim, H. M. I., Lee, S., Zhang, X. H., and Takeuchi, I. (2017). Stability of the oxygen vacancy induced conductivity in $BaSnO_3$ thin films on $SrTiO_3$. *Appl. Phys. Lett.* 111, 172102. doi:10.1063/1.4996548

Jiang, Y. J., Jiang, X. P., Chen, C., Nie, X., Huang, X. K., Jiang, X. A., et al. (2020b). Effect of tantalum substitution on the structural and electrical properties of $BaBi_8Ti_7O_{27}$ intergrowth ceramics. *Ceram. Int.* 46, 8122–8129. doi:10.1016/j.ceramint.2019.12.039

Jiang, Y. J., Jiang, X. P., Chen, C., Nie, X., Huang, X. K., and Zhuang, J. S. (2020a). Structure and electrical characteristics of intergrowth bismuth-layer $((Li_{0.5}Bi_{0.5})_xBa_{1-x}Bi_8Ti_7O_{27}$ ceramics. *J. Chin. Ceram. Soc.* 48 (9), 1376–1382. doi:10.14062/j.issn.0454-5648.20190749

Kobayashi, T., Noguchi, Y., and Miyayama, M. (2004). Polarization properties of superlattice-structured $Bi_4Ti_3O_{12}$-$BaBi_4Ti_4O_{15}$ single crystals and ceramics: Comparison with $Bi_4Ti_3O_{12}$ and $BaBi_4Ti_4O_{15}$. *Jpn. J. Appl. Phys.* 43 (9), 6653–6657. doi:10.1143/jjap.43.6653

Li, X. D., Chen, Z. N., Sheng, L. S., Li, L. L., Bai, W. F., Wen, F., et al. (2019). Remarkable piezoelectric activity and high electrical resistivity in Cu/Nb co-doped $Bi_4Ti_3O_{12}$ high temperature piezoelectric ceramics. *J. Eur. Ceram. Soc.* 39, 2050–2057. doi:10.1016/j.jeurceramsoc.2019.01.042

Lin, Y. Q., and Chen, X. M. (2009). Dielectric relaxations in $Sr_{0.5}Ba_{0.5}Nb_2O_6$/$CoFe_2O_4$ high-ε magnetoelectric composite ceramics. *Mat. Chem. Phys.* 117 (1), 125–130. doi:10.1016/j.matchemphys.2009.05.022

Luo, S., Noguchi, Y., Miyayama, M., and Kudo, T. (2001). Rietveld analysis and dielectric properties of Bi_2WO_6-$Bi_4Ti_3O_{12}$ ferroelectric system. *Mat. Res. Bull.* 36, 531–540. doi:10.1016/s0025-5408(01)00516-5

Ma, H. S., Lee, M. K., Kim, B. H., Park, K. H., Park, J. J., Lee, S. H., et al. (2021). Role of oxygen vacancy defects in piezoelectric thermal stability characteristics of Mn-doped (K, Na, Li)NbO_3 piezoceramics. *Ceram. Int.* 47 (19), 27803–27815. doi:10.1016/j.ceramint.2021.06.207

Macdonald, J. R., and Johnson, W. B. (2005). *Fundamentals of impedance spectroscopy, impedance spectroscopy*. United States: John Wiley & Sons [M].

Majhi, K., Varma, K. B. R., and Rao, K. J. (2009). Possible mechanism of charge transport and dielectric relaxation in SrO-Bi_2O_3-B_2O_3 glasses. *J. Appl. Phys.* 106 (8), 084106. doi:10.1063/1.3246810

Ni, Y., Chen, T. H., Shi, Y. P., He, L. H., and Soh, A. K. (2013). Modeling of polar nanoregions dynamics on the dielectric response of relaxors. *J. Appl. Phys.* 113 (22), 224104. doi:10.1063/1.4809977

Noguchi, Y., Miyayama, M., and Kudo, T. (2000). Ferroelectric properties of intergrowth $Bi_4Ti_3O_{12}$-$SrBi_4Ti_4O_{15}$ ceramics. *Appl. Phys. Lett.* 77 (22), 3639–3641. doi:10.1063/1.1328366

Park, B. H., Kang, B. S., Bu, S. D., Noh, T. W., Lee, J., and Jo, W. (1999). Lanthanum-substituted bismuth titanate for use in non-volatile memories. *Nature* 401, 682–684. doi:10.1038/44352

Pradhani, N., Mahapatra, P. K., and Choudhary, R. N. P. (2018). Effect of cerium oxide addition on optical, electrical and dielectric characteristics of $(Bi_{0.5}Na_{0.5})TiO_3$ ceramics. *J. Phys. Mat.* 1, 015007. doi:10.1088/2515-7639/aacff0

Qi, W. Z., Wang, Y. Q., Wu, J. Y., Hu, Z. M., Jia, C. L., and Zhang, H. T. (2019). Relaxor ferroelectric and photocatalytic properties of $BaBi_4Ti_4O_{15}$. *Adv. Appl. Ceram.* 118 (7), 418–424. doi:10.1080/17436753.2019.1634943

Qiao, X. S., Chen, X. M., Lian, H. L., Zhou, J. P., and Liu, P. (2016). Dielectric, ferroelectric, piezoelectric properties and impedance analysis of nonstoichiometric $(Bi_{0.5}Na_{0.5})_{0.94+x}Ba_{0.06}TiO_3$ ceramics. *J. Eur. Ceram. Soc.* 36 (16), 3995–4001. doi:10.1016/j.jeurceramsoc.2016.06.032

Rafiq, M. A., Rafiq, M. N., and Saravanan, K. V. (2015). Dielectric and impedance spectroscopic studies of lead-free barium-calcium-zirconium-titanium oxide ceramics. *Ceram. Int.* 41 (9), 11436–11444. doi:10.1016/j.ceramint.2015.05.107

Raymond, O., Font, R., Suarez-Almodovar, N., Portelles, J., and Siqueiros, J. M. (2005). Frequency-temperature response of ferroelectromagnetic $Pb(Fe_{1/2}Nb_{1/2})O_3$ ceramics obtained by different precursors. Part II. impedance spectroscopy characterization. *J. Appl. Phys.* 97 (8), 084108. doi:10.1063/1.1870100

Reddy, S. R., Prasad, V. V. B., Bysakh, S., Shanker, V., Hebalkar, N., and Roy, S. K. (2019). Superior energy storage performance and fatigue resistance in ferroelectric BCZT thin films grown in an oxygen-rich atmosphere. *J. Mat. Chem. C* 7, 7073–7082. doi:10.1039/c9tc00569b

Steinsvik, S., Bugge, R., Gjonnes, J., Tafto, J., and Norby, T. (1997). The defect structure of $SrTi_{1-x}Fe_xO_{3-y}$ (x = 0-0.8) investigated by electrical conductivity measurements and electron energy loss spectroscopy (EELS). *J. Phys. Chem. Solids* 58, 969–976. doi:10.1016/s0022-3697(96)00200-4

Suarez, D. Y., Reaney, I. M., and Lee, W. E. (2001). Relation between tolerance factor and T_c in Aurivillius compounds. *J. Mat. Res.* 16 (11), 3139–3149. doi:10.1557/jmr.2001.0433

Tang, Y. X., Shen, Z. Y., Du, Q. X., Zhao, X. Y., Wang, F. F., Qin, X. M., et al. (2018). Enhanced pyroelectric and piezoelectric responses in W/Mn-codoped Bi4Ti3O12 Aurivillius ceramics. *J. Eur. Ceram. Soc.* 38 (16), 5348–5353. doi:10.1016/j.jeurceramsoc.2018.08.025

Tang, Z. K., Xue, Y. F., Teobaldi, G., and Liu, L. M. (2020). The oxygen vacancy in Li-ion battery cathode materials. *Nanoscale Horiz.* 5, 1453–1466. doi:10.1039/d0nh00340a

Tewari, A., Aschauer, U., and Bowen, P. (2014). Atomistic modeling of effect of Mg on oxygen vacancy diffusion in α-alumina. *J. Am. Ceram. Soc.* 97 (8), 2596–2601. doi:10.1111/jace.13008

Wang, C. M., Wang, J. F., Mao, C., Chen, X. F., Dong, X. L., Gai, Z. G., et al. (2008). Enhanced dielectric and piezoelectric properties of aurivillius-type potassium bismuth titanate ceramics by cerium modification. *J. Am. Ceram. Soc.* 91 (9), 3094–3097. doi:10.1111/j.1551-2916.2008.02557.x

Wang, C. M., Wang, J. F., Zhang, S. J., and Shrout, T. R. (2010). Piezoelectric and electromechanical properties of ultrahigh temperature $CaBi_2Nb_2O_9$ ceramics. *Phys. Stat. Sol.* 3, 49–51. doi:10.1002/pssr.200802259

Wang, W., Shan, D., Sun, J. B., Mao, X. Y., and Chen, X. B. (2008). Aliovalent B-site modification on three- and four-layer Aurivillius intergrowth. *J. Appl. Phys.* 103, 044102. doi:10.1063/1.2838486

Wang, Y. Y., Chen, Y., and Zheng, D. Y. (2022). Development of multifunctional electronic-ceramics with piezoelectric effect and varistor behavior. *Ceram. Int.* 48, 26818–26827. doi:10.1016/j.ceramint.2022.05.383

Wong, Y. J., Hassan, J., Chen, S. K., and Ismail, I. (2017). Combined effects of thermal treatment and Er-substitution on phase formation, microstructure, and dielectric responses of $Bi_4Ti_3O_{12}$ Aurivillius ceramics. *J. Alloys Compd.* 723, 567–579. doi:10.1016/j.jallcom.2017.06.268

Wu, B., Ma, J., Wu, W., and Chen, M. (2018). Evolution of microstructure and electrical properties of Aurivillius phase $(CaBi_4Ti_4O_{15})_{1-x}(Bi_4Ti_3O_{12})_x$ ceramics. *Ceram. Int.* 44 (8), 9168–9173. doi:10.1016/j.ceramint.2018.02.125

Wu, J., and Wang, J. (2010). Ferroelectric and impedance behavior of La- and Ti-codoped $BiFeO_3$ thin films. *J. Am. Ceram. Soc.* 93, 2795–2803. doi:10.1111/j.1551-2916.2010.03816.x

Xie, X. C., Wang, T. Z., Zhou, Z. Y., Cheng, G. F., Liang, R. H., and Dong, X. L. (2019). Enhanced piezoelectric properties and temperature stability of $Bi_4Ti_3O_{12}$-based Aurivillius ceramics via W/Nb substitution. *J. Eur. Ceram. Soc.* 39, 957–962. doi:10.1016/j.jeurceramsoc.2018.12.061

Yang, H., Chen, Z. Z., Peng, R. R., Huang, H. L., Fu, Z. P., Zhai, X. F., et al. (2018). Superlattice-like structure and enhanced ferroelectric properties of intergrowth Aurivillius oxides. *RSC Adv.* 8 (30), 16937–16946. doi:10.1039/c8ra02374c

Yoo, D. Y., Chong, E., Kim, D. H., Ju, B. K., and Lee, S. Y. (2012). Effect of magnesium oxide passivation on the performance of amorphous indium-gallium-zinc-oxide thin film transistors. *Thin Solid Films* 520, 3783–3786. doi:10.1016/j.tsf.2011.10.065

Yu, G. B., Wang, L. G., Zhu, C. M., Lv, F. Z., Liu, F. C., Kong, W. J., et al. (2020). Relaxor dielectric properties of lead-free $Bi_4Ti_3O_{12}/Bi_{4.5}Na_{0.5}Ti_4O_{15}$ intergrowth ceramics. *Ceram. Int.* 46, 9474–9484. doi:10.1016/j.ceramint.2019.12.208

Zhang, L. N., Li, G. R., Zhao, S. C., Zheng, L. Y., and Yin, Q. R. (2005). Electrical behavior of $Bi_4Ti_3O_{12}$ layer-structured ferroelectric ceramics. *J. Inorg. Mat.* 20, 1389–1395. doi:10.3321/j.issn:1000-324X.2005.06.020

Zhang, S. J., Xia, R., Lebrun, L., Anderson, D., and Shrout, T. R. (2005). Piezoelectric materials for high power, high temperature applications. *Mat. Lett.* 59, 3471–3475. doi:10.1016/j.matlet.2005.06.016

Zhang, S. J., and Yu, F. P. (2011). Piezoelectric materials for high temperature sensors. *J. Am. Ceram. Soc.* 94 (10), 3153–3170. doi:10.1111/j.1551-2916.2011.04792.x